Renormalization Group Study of Hidden Symmetry in Twisted Bilayer Graphene with Coulomb Interactions

Oskar Vafek [1,2,*] and Jian Kang [3,†]

[1] National High Magnetic Field Laboratory, Tallahassee, Florida 32310, USA
[2] Department of Physics, Florida State University, Tallahassee, Florida 32306, USA
[3] School of Physical Science and Technology & Institute for Advanced Study, Soochow University, Suzhou 215006, China

(Received 15 September 2020; accepted 19 November 2020; published 18 December 2020)

We develop a two stage renormalization group which connects the continuum Hamiltonian for twisted bilayer graphene at length scales shorter than the moire superlattice period to the Hamiltonian for the active narrow bands only which is valid at distances much longer than the moire period. In the first stage, the Coulomb interaction renormalizes the Fermi velocity and the interlayer tunnelings in such a way as to suppress the ratio of the same sublattice to opposite sublatice tunneling, hence approaching the so-called chiral limit. In the second stage, the interlayer tunneling is treated nonperturbatively. Via a progressive numerical elimination of remote bands the relative strength of the one-particle-like dispersion and the interactions within the active narrow band Hamiltonian is determined, thus quantifying the residual correlations and justifying the strong coupling approach in the final step. We also calculate exactly the exciton energy spectrum from the Coloumb interactions projected onto the renormalized narrow bands. The resulting softening of the collective modes marks the propinquity of the enlarged ("hidden") $U(4)\times U(4)$ symmetry in the magic angle twisted bilayer graphene.

DOI: 10.1103/PhysRevLett.125.257602

It has been known for some time that electron-electron Coulomb interactions cause an upward renormalization of the Fermi velocity, v_F, upon approaching the charge neutrality point (CNP) of monolayer graphene [1–7]. Such momentum dependent steepening of the Dirac cone depends on the graphene's dielectric environment and is weaker for stronger dielectrics, but even for hexagonal boron nitride (HBN) encapsulated devices the increase can be [2] ~10%–15%. Such a small change in v_F would be of limited interest if it weren't for the recent explosion of research into the magic angle [8] twisted bilayer graphene (TBG) [9–77], where the experiments show extremely strong sensitivity of the correlated electron phenomena to the twist angle θ. Even a ~5% change of θ away from the optimal (magic) value has been reported to produce at least a factor of 2 reduction [23,24] of the superconducting T_c, with even stronger suppression of the correlated insulator states [23].

The strong band structure sensitivity is due to the dependence on the dimensionless parameters $w_{0,1}/v_F k_\theta$, where w_0 and w_1 parameterize the interlayer tunneling energy in the AA and AB regions, respectively, and where the momentum displacement of the Dirac cones is given by $k_\theta = 2k_D \sin\frac{\theta}{2}$, $k_D = 4\pi/3a_0$, $a_0 \approx 0.246$ nm (in $\hbar = 1$ units) [8]. Therefore, at a fixed magic θ, even a ~10% difference in v_F alone would be sufficient to detune the system from the optimal flat band condition. As such, if neither of w_j renormalized due to Coulomb interactions, but only v_F did, the magic angle condition would depend on whether the TBG was encapsulated in HBN, or only from one side, because the different dielectric environments would produce a different strength of Coulomb interactions, the former with a dielectric constant [48,78] $\epsilon_{\mathrm{HBN}} \approx 4.4$ and the latter with $\epsilon \approx (1+\epsilon_{\mathrm{HBN}})/2 = 2.7$. The difference in the v_F, and therefore the magic angle, would then be within the sensitivity of the correlated insulating states; no such dependence of the magic angle on the partial or complete encapsulation has been reported.

Here we develop a renormalization group (RG) approach to the Coulomb interactions in the twisted bilayer graphene and show that w_1 renormalizes in precisely such a way as to compensate for the growth of v_F making the magic angle largely insensitive to the effective dielectric constant ϵ. Interestingly, we find that w_0 does not renormalize due to Coulomb interactions. Therefore, the ratio w_0/w_1 shrinks and the system flows closer to the chiral limit described by Tarnopolsky, Kruchkov, and Vishvanath [47]. As illustrated in Fig. 1(c), the flow from a high energy (with the UV cutoff E_c), where the Coulomb interaction and $w_{0,1}$ are perturbative, to a low energy of the narrow bands where neither is, crosses over to a regime where the effects of $w_{0,1}$ become nonperturbative, but the Coulomb interaction is still perturbative. This happens at the energy scale $E_c^* \sim \mathcal{O}(w_1)$, marking the beginning of the second stage of our RG; the band structure scaling collapse in Fig. 2 shows that the second stage seamlessly connects to the first stage even if E_c^* changes. In the second stage, we numerically integrate out the two most remote bands, one above

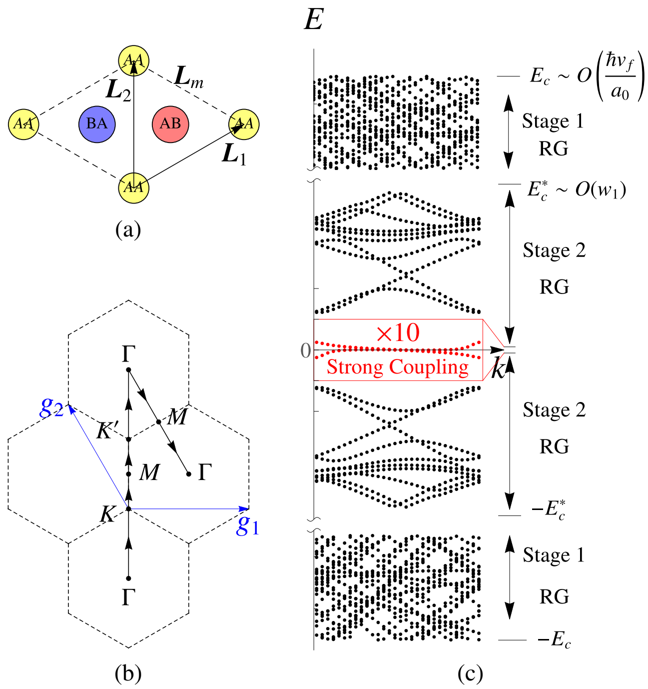

FIG. 1. (a) Moire lattice with lattice spacing L_m. (b) Moire Brillouin zone. (c) Schematic illustration of the two stage RG procedure for arriving at the strong coupling limit. In the stage 1, both the Coulomb interaction and the moire potential are perturbative, in the stage 2 only the Couloumb interaction is. In the final step, when only the narrow bands (red) remain, the interaction is the largest scale.

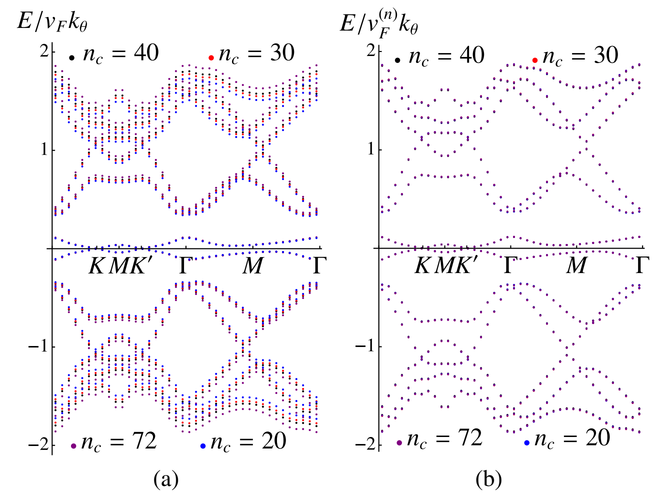

FIG. 2. (a) Low energy spectra after $n_c - 5$ steps of the stage 2 RG for $n_c = 72$ (purple), 40 (black), 30 (red), 20 (blue). At n_c, each starts with the same Fermi velocity, v_F, in the BM model at $w_1/v_F k_\theta = 0.5$, but with $w_0/w_1 = 0.83$ (purple), 0.805 (black), 0.787 (red), and 0.768 (blue). The values are chosen based on the dielectric constant $\epsilon = 4.4$ and scaling in Eq. (18) and the cutoff energies set by the nth band maxima at $n_c = 72$. (b) Results of the panel (a) rescaled by $v_F^{(n)} = v_F/[1 + (e^2/4\epsilon v_F)\ln(E_c/E_c^*)]$ for E_c set by the band maximum at $n_c = 72$, demonstrating the scaling collapse and thus independence of the results of stage 2 RG on E_c^*.

and one below the CNP, rotate the remaining states to diagonalize the renormalized kinetic energy, and reexpress the interaction in terms of the rotated states, iterating the procedure until we reach the narrow bands. If the resulting narrow bands' bandwidth (or, more precisely the root mean square of the renormalized kinetic energy dispersion) is much smaller than the interaction (or more precisely, the particle-hole charge gap), as we find it is near the magic angle, the final step is treated nonperturbatively in the Coulomb interaction, i.e., by solving the interaction-only problem (strong coupling limit) and then treating the renormalized kinetic energy terms as a perturbation.

The condition $w_0 = 0$, and thus the chiral limit [47,79,80], was previously thought to be unrealistic and the value $w_0/w_1 \sim 0.8$ was taken from density functional theory-like calculations [28,50,81]. Our results [Eqs. (17) and (18)] show that for the Coulomb interacting system, the chiral limit becomes exact near the CNP in the limit $E_c/w_1 \to \infty$, albeit approaching logarithmically. This has important consequences for the effective residual interaction in the narrow band, because of the increased sublattice polarization of the narrow band wave functions [67]. We find additional enhancement of the sublattice polarization after the second stage, as well as steepening of the Wilson loop eigenvalues [42], indicating an additional approach to the chiral limit during the second stage RG.

The dominant part of the Coulomb interaction Hamiltonian projected onto perfectly sublattice polarized chiral limit narrow bands is invariant under a larger symmetry, $U(4) \times U(4)$, than for $w_0/w_1 \neq 0$, $U(4)$, when particle-hole (p-h) symmetry [42] is exact [67]. This symmetry enhancement enlarges the manifold of nearly degenerate correlated states [67]. Our exact calculation of the collective mode spectrum in the strong coupling limit indeed shows not only four Goldstone bosons associated with the $U(4)$ spin-valley ferromagnetism [48,67], but also a softening of four additional collective modes, indicating the approach to the $U(4) \times U(4)$ ferromagnet [67] with its eight Goldstone bosons (see Fig. 3).

We begin with the Hamiltonian $H = H_{\rm kin} + V_{\rm int}$ where

$$H_{\rm kin} = \int d^2\mathbf{r}\chi_\sigma^\dagger(\mathbf{r})\begin{pmatrix} \hat{H}_{\rm BM} & 0 \\ 0 & \hat{H}^*_{\rm BM}\end{pmatrix}\chi_\sigma(\mathbf{r}) \qquad (1)$$

$$V_{\rm int} = \frac{1}{2}\int d^2\mathbf{r}d^2\mathbf{r}' V(\mathbf{r}-\mathbf{r}')\chi_\sigma^\dagger(\mathbf{r})\chi_{\sigma'}^\dagger(\mathbf{r}')\chi_{\sigma'}(\mathbf{r}')\chi_\sigma(\mathbf{r}) \qquad (2)$$

where $\chi_\sigma^\dagger = (\psi_\sigma^\dagger, \phi_\sigma^\dagger)$ creates an electron in valley $\mathbf{K}$ ($\mathbf{K}'$) for its upper (lower) component, and the repeated spin-$\frac{1}{2}$ indices σ are summed. The Bistritzer-MacDonald [8] (BM) continuum Hamiltonian [28,29,40,42,47] for twist angle θ is

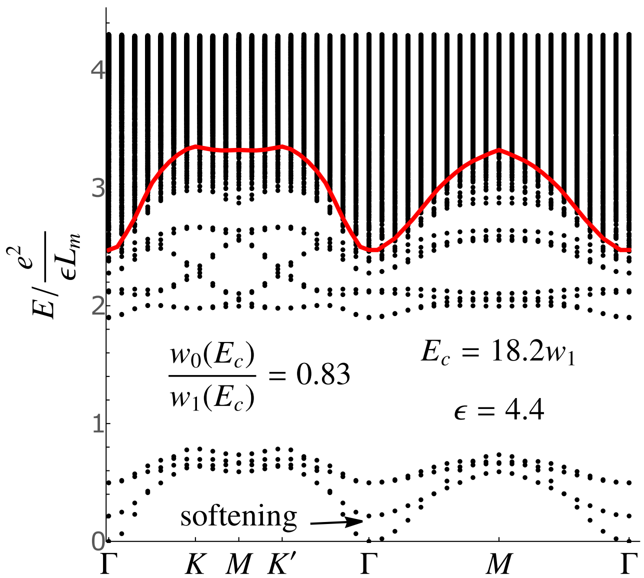

FIG. 3. The strong coupling exciton spectrum after stage 1 and 2 RG, starting the stage 1 with $E_c = 18.2w_1$ corresponding to 2 eV for $w_1 = 110$ meV, $w_1/(v_F k_\theta) = 0.586$ (magic angle), and the initial $w_0/w_1 = 0.83$. The branch that becomes gapless at $\mathbf{\Gamma}$ corresponds to four Goldstone modes of the $U(4)$ spin-valley ferromagnet with quadratic dispersion. Another branch, emphasized by the arrow, softens during the RG, eventually also becoming gapless in the chiral limit, with a total of eight Goldstone modes of the $U(4)\times U(4)$ ferromagnet. The red curve is the onset of the particle-hole continuum.

$$\hat{H}_{\rm BM} = \begin{pmatrix} v_F \sigma_{\frac{\theta}{2}}\cdot\mathbf{p} & T(\mathbf{r}) \\ T^\dagger(\mathbf{r}) & v_F\sigma_{-\frac{\theta}{2}}\cdot\mathbf{p} \end{pmatrix}, \tag{3}$$

where the twisted Pauli matrices acting on the sublattice indices are $\sigma_{\frac{\theta}{2}} = e^{-\frac{i}{4}\theta\sigma_z}(\sigma_x,\sigma_y)e^{\frac{i}{4}\theta\sigma_z}$, $\mathbf{q}_1 = k_\theta(0,-1)$, $\mathbf{q}_{2,3} = k_\theta[(\pm\sqrt{3}/2),(1/2)]$. The interlayer hopping $T(\mathbf{r}) = \sum_{j=1}^3 T_j e^{-i\mathbf{q}_j\cdot\mathbf{r}}$ is controlled by two parameters $w_{0,1}$ via

$$T_{j+1} = w_0 1_2 + w_1\left[\cos\left(\frac{2\pi}{3}j\right)\sigma_x + \sin\left(\frac{2\pi}{3}j\right)\sigma_y\right], \tag{4}$$

where 1_n is an $n\times n$ unit matrix. $\hat{H}_{\rm BM}$ acts on its eigenfunctions

$$\Psi_{n,\mathbf{k}}(\mathbf{r}) = \sum_{\mathbf{g}}\begin{pmatrix} a_{n,\mathbf{g}}(\mathbf{k}) \\ b_{n,\mathbf{g}}(\mathbf{k})e^{i\mathbf{q}_1\cdot\mathbf{r}}\end{pmatrix} e^{i\mathbf{k}\cdot\mathbf{r}}e^{i\mathbf{g}\cdot\mathbf{r}}, \tag{5}$$

where $\mathbf{g} = m_1\mathbf{g}_1 + m_2\mathbf{g}_2$ for integer $m_{1,2}$ and $\mathbf{g}_{1,2} = \mathbf{q}_{2,3} - \mathbf{q}_1$. The slow fields at the two valleys $\mathbf{K}/\mathbf{K}'$ are expanded in the "band" basis fermion annihilation operators $d_{\sigma,\mathbf{K}/\mathbf{K}',n,\mathbf{k}}$ with crystal momentum $\mathbf{k}$ in the first moire Brillouin zone, and the band index n as

$$\chi_\sigma(\mathbf{r}) = \begin{pmatrix}\psi_\sigma(\mathbf{r}) \\ \phi_\sigma(\mathbf{r})\end{pmatrix} = \sum_{n\mathbf{k}}\begin{pmatrix}\Psi_{n,\mathbf{k}}(\mathbf{r})d_{\sigma,\mathbf{K},n,\mathbf{k}} \\ \Psi^*_{n,\mathbf{k}}(\mathbf{r})d_{\sigma,\mathbf{K}',n,-\mathbf{k}-\mathbf{q}_1}\end{pmatrix}. \tag{6}$$

It will be helpful for us to think about $H_{\rm kin}$ as a lowest order gradient expansion of a continuum field theory [40], with coupling constants that can flow due to $V_{\rm int}$ under the first stage of the RG.

As pointed out in Ref. [42], if the small angle rotation in $\sigma_{\theta/2}$ is ignored, then $\hat{H}_{\rm BM}$ enjoys a p-h symmetry for any value of w_0 and w_1,

$$-i\mu_y\sigma_x\hat{H}^*_{\rm BM}\sigma_x i\mu_y = -\hat{H}_{\rm BM}, \tag{7}$$

in that if $\Psi_{n,\mathbf{k}}(\mathbf{r})$ is an eigenstate of $\hat{H}_{\rm BM}$ at $\mathbf{k}$ with eigenvalue $\epsilon_{n,\mathbf{k}}$, then $-i\mu_y\sigma_x\Psi^*_{n,\mathbf{k}}(\mathbf{r})$ is an eigenstate at $-\mathbf{k}-\mathbf{q}_1$ with eigenvalue $-\epsilon_{n,\mathbf{k}}$. In what follows, we will neglect the small p-h asymmetric term which is 2 orders of magnitude smaller than $w_{0,1}$ and which we analyze in Ref. [82], and perform our RG assuming this approximate symmetry is present.

Up to an overall shift of the chemical potential, we can rewrite $V_{\rm int}$ as

$$V_{\rm int} = \frac{1}{2}\int d^2\mathbf{r}d^2\mathbf{r}'V(\mathbf{r}-\mathbf{r}')\delta\rho(\mathbf{r})\delta\rho(\mathbf{r}'), \tag{8}$$

$$\delta\rho(\mathbf{r}) = \chi^\dagger_\sigma(\mathbf{r})\chi_\sigma(\mathbf{r}) - \frac{1}{2}\{\chi^\dagger_\sigma(\mathbf{r}),\chi_\sigma(\mathbf{r})\}. \tag{9}$$

For a pure Coulomb interaction $V(\mathbf{r}) = e^2/\epsilon r$. The Hamiltonian in Eqs. (1) and (2) is defined at some high energy cutoff $\pm E_c$ which corresponds to a maximal value of the band index n_c in our expansion. The parameters v_F, w_0, and w_1 should also be thought of as being fixed by a measurement at E_c. The last term in Eq. (9) is usually ignored, but for our RG, it will be helpful to express it as $\frac{1}{2}\{\chi^\dagger_\sigma(\mathbf{r}),\chi_\sigma(\mathbf{r})\} =$

$$\bar{\rho}_{E_c}(\mathbf{r}) = 2\sum_{|\epsilon_{n\mathbf{k}}|\le E_c}\Psi^*_{n,\mathbf{k}}(\mathbf{r})\Psi_{n,\mathbf{k}}(\mathbf{r}). \tag{10}$$

In the first stage, we split $\chi_\sigma(\mathbf{r}) = \chi^>_\sigma(\mathbf{r}) + \chi^<_\sigma(\mathbf{r})$ and integrate out the fast modes $\chi^>_\sigma(\mathbf{r})$ with kinetic energy $E'_c < |\epsilon_{n,\mathbf{k}}| \le E_c$, such that $E'_c \gg w_{0,1}$. In this regime, the $V_{\rm int}$ can be treated perturbatively. Its contribution to the slow mode Hamiltonian is then

$$\begin{aligned} V_{\rm int} \to & \frac{1}{2}\int d^2\mathbf{r}d^2\mathbf{r}'V(\mathbf{r}-\mathbf{r}')\delta\rho^<(\mathbf{r})\delta\rho^<(\mathbf{r}') \\ & + \frac{1}{2}\int d^2\mathbf{r}d^2\mathbf{r}'V(\mathbf{r}-\mathbf{r}')\chi^{<\dagger}_\sigma(\mathbf{r})\delta\mathcal{F}(\mathbf{r},\mathbf{r}')\chi^<_\sigma(\mathbf{r}'), \end{aligned} \tag{11}$$

where $\delta\rho^<(\mathbf{r}) = \chi^{<\dagger}_\sigma(\mathbf{r})\chi^<_\sigma(\mathbf{r}) - \bar{\rho}_{E'_c}(\mathbf{r})$ which follows from the p-h symmetry. The correction to the $\hat{H}_{\rm BM}$ comes from

$$\delta\mathcal{F}(\mathbf{r},\mathbf{r}') = \sum_{E'_c<|\epsilon_{n\mathbf{k}}|\le E_c} \mathrm{sign}(\epsilon_{n\mathbf{k}}) \begin{pmatrix} f_{n,\mathbf{k}}(\mathbf{r},\mathbf{r}') & 0 \\ 0 & f^*_{n,\mathbf{k}}(\mathbf{r},\mathbf{r}') \end{pmatrix}, \tag{12}$$

where $f_{n,\mathbf{k}}(\mathbf{r},\mathbf{r}') = \Psi_{n,\mathbf{k}}(\mathbf{r})\Psi^\dagger_{n,\mathbf{k}}(\mathbf{r}')$. We can now write

$$\sum_{E'_c<|\epsilon_{n\mathbf{k}}|\le E_c} \mathrm{sign}(\epsilon_{n\mathbf{k}}) f_{n,\mathbf{k}}(\mathbf{r},\mathbf{r}') = \oint_{\mathcal{C}} \frac{dz}{2\pi i}\langle\mathbf{r}|\hat{G}(z)|\mathbf{r}'\rangle \tag{13}$$

where $\hat{G}(z) = (z - \hat{H}_{\mathrm{BM}})^{-1}$, and the contour $\mathcal{C}$ encloses the z-plane real line segment $(-E_c, -E'_c)$ in the clockwise, and segment (E'_c, E_c) in the counterclockwise, sense. As long as $E'_c \gg w_{0,1}$, the dominant contribution to the contour integral can be found by replacing $\hat{G}(z) \approx \hat{G}_0(z) + \hat{G}_0(z)\hat{T}\hat{G}_0(z) + \mathcal{O}(w^2_{0,1}/E'^2_c)$. For small $E_c - E'_c$, we thus find that in the first RG stage [82],

$$\frac{dv_F}{d\ln E_c} = -\frac{e^2}{4\epsilon}, \tag{14}$$

$$\frac{dw_0}{d\ln E_c} = 0, \tag{15}$$

$$\frac{dw_1}{d\ln E_c} = -w_1\frac{e^2}{4\epsilon v_F}, \tag{16}$$

and e^2, being the prefactor of a nonanalytic term, does not renormalize when high energy modes are eliminated [83]. Integrating the above equations, i.e., progressively reducing the cutoff to E^*_c gives

$$\frac{w_1(E^*_c)}{v_F(E^*_c)} = \frac{w_1(E_c)}{v_F(E_c)}, \tag{17}$$

$$\frac{w_0(E^*_c)}{w_1(E^*_c)} = \frac{w_0(E_c)}{w_1(E_c)} \Bigg/ \left(1 + \frac{e^2}{4\epsilon v_F(E_c)}\ln\frac{E_c}{E^*_c}\right). \tag{18}$$

Equation (17) implies that the magic angle condition is largely insensitive to the renormalization. Equation (18) shows that even if we start away from the chiral limit [47] at the UV scale E_c, at a lower energy scale E^*_c we approach it. Next, we combine this stage 1 RG with the nonperturbative (in moire potential) stage 2 numerical RG at $6w_1 \gtrsim E^*_c$, but we stress that results are insensitive to the choice of E^*_c as long as $w_{1,0}/E^*_c$ is small so that stage 1 is under control. The scaling collapse of the band structure shown in the Fig. 2 demonstrates this insensitivity for $w_1/v_F k_\theta = 0.5$, $e^2/v_F = 2.2$, and $\epsilon = 4.4$ with several choices of n_c. We also find an increase of the sublattice polarization and steepening of the Wilson loops along the RG evolution [82], indicating a further approach of the chiral limit during stage 2.

Note that at each step of our procedure we rediagonalize the BM-like model in the subspace of the low energy bands corrected by V_{int}. We also reexpress the V_{int} in Eq. (8) in terms of the current (rotated) eigenstates of the BM model below the running energy cutoff, and because $\bar{\rho}_{E'_c}(\mathbf{r})$ is invariant under the basis rotation, the p-h symmetry is explicitly preserved. After the final step, we are thus left with two renormalized narrow bands per valley, and V_{int} containing $\rho(\mathbf{r})$ and $\bar{\rho}_0(\mathbf{r})$ both expressed in terms of the final renormalized wave functions $\tilde{\Psi}_{n\pm,\mathbf{k}}(\mathbf{r})$, with the upper and lower bands denoted by $n+$ and $n-$, respectively. Because the p-h symmetry is preserved during this procedure, we can choose $\tilde{\Psi}_{n-,\mathbf{k}}(\mathbf{r}) = -i\mu_y\sigma_x\tilde{\Psi}^*_{n+,-\mathbf{k}-\mathbf{q}_1}(\mathbf{r})$. Substitution of such field operators Eq. (6) gives $\rho(\mathbf{r}) = \sum_{\mathbf{k}\mathbf{k}'}\sum_{\sigma=\uparrow,\downarrow} D^\dagger_{\mathbf{k}\sigma}\mathcal{P}_{\mathbf{k}\mathbf{k}'}(\mathbf{r})D_{\mathbf{k}'\sigma}$, where within the narrow band $D^\dagger_{\mathbf{k}\sigma} = (d^\dagger_{\mathbf{K},n+,\mathbf{k}\sigma}, d^\dagger_{\mathbf{K},n-,\mathbf{k}\sigma}, d^\dagger_{\mathbf{K}',n+,\mathbf{k}\sigma}, d^\dagger_{\mathbf{K}',n-,\mathbf{k}\sigma})$. Suppressing $\mathbf{k}\mathbf{k}'$ and $\mathbf{r}$ dependence, $\mathcal{P} = b_0 1_4 + b_1\tau_3\tilde{\sigma}_1 + b_2 1_2\tilde{\sigma}_2 + b_3\tau_3\tilde{\sigma}_3$, thus commuting with all 16 generators of spin-valley $U(4)$ symmetry [67] $1_4 s_\mu$, $\tau_3 1_2 s_\mu$, $\tau_2\tilde{\sigma}_2 s_\mu$, $\tau_1\tilde{\sigma}_2 s_\mu$, where $\mu = 0$, 1, 2, 3 and τ acts on valley, $\tilde{\sigma}$ on band, and s on spin components ($s_0 = 1_2$).

If a state $|\Omega\rangle$ is annihilated by $\delta\rho(\mathbf{r})$ for all $\mathbf{r}$, then it is a ground state at the strong coupling because V_{int} is positive definite [48,67]. Moreover, any state obtained by a global $U(4)$ rotation is also a ground state, and, at the CNP, can be obtained from a fully filled valley polarized state [48,67]. The exact n-body excitations above any one ground state can also be obtained by solving an $(n-1)$-body problem because $V_{\mathrm{int}}X|\Omega\rangle = \frac{1}{2}\int d^2\mathbf{r}d^2\mathbf{r}' V(\mathbf{r}-\mathbf{r}')\{\delta\rho(\mathbf{r}),[\delta\rho(\mathbf{r}'),X]\}|\Omega\rangle$ and because the center of mass momentum is conserved. Therefore, solving the operator eigenequation

$$\mathrm{E}X = \frac{1}{2}\int d^2\mathbf{r}d^2\mathbf{r}' V(\mathbf{r}-\mathbf{r}')\{\delta\rho(\mathbf{r}),[\delta\rho(\mathbf{r}'),X]\}, \tag{19}$$

provides the exact excitation states in the strong coupling limit. Equation (19) can be readily solved for a single particle excitation and we show the result in Ref. [82]. Here we focus on the charge neutral excitations (excitons) $X = \sum_{mm'\mathbf{k}} f^{\alpha\beta}_{mm'\mathbf{k}}(\mathbf{q}) d^\dagger_{\alpha m,\mathbf{k}} d_{\beta m',(\mathbf{k}-\mathbf{q})\ \mathrm{mod}\ \mathbf{g}}$, with spin and valley labels α, β, by finding the eigenfunctions $f^{\alpha\beta}_{mm'\mathbf{k}}(\mathbf{q})$. Because of the spin-valley $U(4)$ invariance of these equations, it is sufficient to solve for one spin and valley projection, the rest can be obtained by the symmetry. The numerically obtained exciton spectrum at the magic angle is shown in Fig. 3 for the center of mass momentum $\mathbf{q}$ along the path shown in Fig. 1(b). The quadratically vanishing dispersion of the lowest branch corresponds to the four $U(4)$ ferromagnetic Goldstone bosons [84]. Under the RG a second set of four modes softens. This corresponds to approaching the ("hidden") $U(4)\times U(4)$ invariant chiral limit [67] with its eight Goldstone bosons. Their gap is a measure of the $U(4)\times U(4)$ anisotropy terms and for the parameters in the Fig. 3 this gap is $\Delta_{U(4)\times U(4)} \approx 0.2e^2/\epsilon L_m \sim 5$ meV; the gap vanishes at the chiral limit. Note that the modes disperse despite a complete absence of kinetic energy terms due to the nonlocal structure of the projected density operators [48].

The H_{kin} breaks the spin-valley $U(4)$ symmetry down to $U(2)\times U(2)$ and causes splitting of the degenerate ground state manifold. We can obtain an upper bound on the resulting anisotropy terms from second order perturbation in (renormalized) kinetic energy (i.e., "superexchange") by replacing the energy of the excited states at $\mathbf{\Gamma}$ with the lowest energy exciton that has a nonzero overlap on the kinetic energy operator ($E_{ph}^{\min}\approx 2e^2/\epsilon L_m$ for Fig. 3). For a spin independent valley rotation, parameterized by three Euler angles, $e^{\frac{i}{2}\alpha\tau_3 1_4}e^{\frac{i}{2}\omega\tau_2\sigma_2 1_2}e^{\frac{i}{2}\gamma\tau_3 1_4}$ we find that the energy splitting per unit cell, $\Delta_{U(4)}$, is bounded from above by $-(\sin^2\omega)4\int d^2\mathbf{k}\epsilon^2_{n+,\mathbf{k}}/(A_{\mathrm{BZ}}E_{ph}^{\min})$. The lowest energy state for such a rotation is the Kramers intervalley coherent state [67] at $\omega=\frac{\pi}{2}$. For the parameters in Fig. 3, we find that $\Delta_{U(4)}<6.7\times 10^{-3}e^2/\epsilon L_m\sim 0.17$ meV, justifying the strong coupling approach.

The theory presented here can be extended to include the RPA effects and the p-h asymmetry, which will be important for any detailed quantitative comparison with experiments. Nevertheless, the Coulomb RG induced softening of the hidden symmetry collective modes, whose natural energy scale would normally be $\sim e^2/\epsilon L_m\sim 25$ meV, suggests that they may not be frozen out even at $\sim$50 K. Finally, our results offer a significant shift of perspective in that the chiral limit [47]—previously considered unphysical—gains the status of an attractive mid-IR RG fixed point when $E_c/w_1\to\infty$.

We would like to thank Professor B. Andrei Bernevig for valuable discussions and for sharing their unpublished results with us. O. V. is supported by NSF DMR-1916958 and partially by the National High Magnetic Field Laboratory through NSF Grant No. DMR-1157490 and the State of Florida. J. K. is supported by Priority Academic Program Development (PAPD) of Jiangsu Higher Education Institutions.

*vafek@magnet.fsu.edu
†jkang@suda.edu.cn

[1] D. C. Elias *et al.*, Dirac cones reshaped by interaction effects in suspended graphene, Nat. Phys. **7**, 701 (2011).
[2] G. L. Yu *et al.*, Interaction phenomena in graphene seen through quantum capacitance, Proc. Natl. Acad. Sci. U.S.A. **110**, 3282 (2013).
[3] J. Gonzalez, F. Guinea, and A. H. Vozmediano, Non-Fermi liquid behavior of electrons in the half-filled honeycomb lattice (A renormalization group approach), Nucl. Phys. **B424**, 595 (1994).
[4] O. Vafek, Anomalous Thermodynamics of Coulomb-Interacting Massless Dirac Fermions in Two Spatial Dimensions, Phys. Rev. Lett. **98**, 216401 (2007).
[5] D. E. Sheehy and J. Schmalian, Quantum Critical Scaling in Graphene, Phys. Rev. Lett. **99**, 226803 (2007).
[6] G. Borghi, M. Polini, R. Asgari, and A. H. MacDonald, Fermi velocity enhancement in monolayer and bilayer graphene, Solid State Commun. **149**, 1117 (2009).
[7] E. Barnes, E. H. Hwang, R. E. Throckmorton, and S. Das Sarma, Effective field theory, three-loop perturbative expansion, and their experimental implications in graphene many-body effects, Phys. Rev. B **89**, 235431 (2014).
[8] R. Bistritzer and A. H. MacDonald, Moire bands in twisted double-layer graphene, Proc. Natl. Acad. Sci. U.S.A. **108**, 12233 (2011).
[9] Y. Cao, V. Fatemi, A. Demir, S. Fang, S. L. Tomarken, J. Y. Luo, J. D. Sanchez-Yamagishi, K. Watanabe, T. Taniguchi, E. Kaxiras, R. C. Ashoori, and P. Jarillo-Herrero, Correlated insulator behaviour at half-filling in magic-angle graphene superlattices, Nature (London) **556**, 43 (2018).
[10] Y. Cao, V. Fatemi, S. Fang, K. Watanabe, T. Taniguchi, E. Kaxiras, and P. Jarillo-Herrero, Unconventional superconductivity in magic-angle graphene superlattices, Nature (London) **556**, 80 (2018).
[11] M. Yankowitz, S. Chen, H. Polshyn, Y. Zhang, K. Watanabe, T. Taniguchi, D. Graf, A. F. Young, and C. R. Dean, Tuning superconductivity in twisted bilayer graphene, Science **363**, 1059 (2019).
[12] A. L. Sharpe, E. J. Fox, A. W. Barnard, J. Finney, K. Watanabe, T. Taniguchi, M. A. Kastner, and D. Goldhaber-Gordon, Emergent ferromagnetism near three-quarters filling in twisted bilayer graphene, Science **365**, 605 (2019).
[13] M. Serlin, C. L. Tschirhart, H. Polshyn, Y. Zhang, J. Zhu, K. Watanabe, T. Taniguchi, L. Balents, and A. F. Young, Intrinsic quantized anomalous hall effect in a Moire heterostructure, Science **367**, 900 (2019).
[14] A. Kerelsky, L. J. McGilly, D. M. Kennes, L. Xian, M. Yankowitz, S. Chen, K. Watanabe, T. Taniguchi, J. Hone, C. Dean *et al.*, Maximized electron interactions at the magic angle in twisted bilayer graphene, Nature (London) **572**, 95 (2019).
[15] X. Lu, P. Stepanov, W. Yang, M. Xie, M. A. Aamir, I. Das, C. Urgell, K. Watanabe, T. Taniguchi, G. Zhang, A. Bachtold, A. H. MacDonald, and D. K. Efetov, Superconductors, orbital magnets and correlated states in magic-angle bilayer graphene, Nature (London) **574**, 653 (2019).
[16] Y. Xie, B. Lian, B. Jack, X. Liu, C.-L. Chiu, K. Watanabe, T. Taniguchi, B. A. Bernevig, and A. Yazdani, Spectroscopic signatures of many body correlations in magic-angle twisted bilayer graphene, Nature (London) **572**, 101 (2019).
[17] S. L. Tomarken, Y. Cao, A. Demir, K. Watanabe, T. Taniguchi, P. Jarillo-Herrero, and R. C. Ashoori, Electronic Compressibility of Magic-Angle Graphene Superlattices, Phys. Rev. Lett. **123**, 046601 (2019).
[18] Y. Jiang, X. Lai, K. Watanabe, T. Taniguchi, K. Haule, J. Mao, and E. Y. Andrei, Charge order and broken rotational symmetry in magic-angle twisted bilayer graphene, Nature (London) **573**, 91 (2019).
[19] Y. Choi, J. Kemmer, Y. Peng, A. Thomson, H. Arora, R. Polski, Y. Zhang, H. Ren, J. Alicea, G. Refael, F. von Oppen, K. Watanabe, T. Taniguchi, and S. Nadj-Perge, Electronic correlations in twisted bilayer graphene near the magic angle, Nat. Phys. **15**, 1174 (2019).

[20] P. Stepanov, I. Das, X. Lu, A. Fahimniya, K. Watanabe, T. Taniguchi, F. H. L. Koppens, J. Lischner, L. Levitov, and D. K. Efetov, Untying the insulating and superconducting orders in magic-angle graphene, Nature (London) **583**, 375 (2020).
[21] D. Wong, K. P. Nuckolls, M. Oh, B. Lian, Y. Xie, S. Jeon, K. Watanabe, T. Taniguchi, B. A. Bernevig, and A. Yazdani, Cascade of electronic transitions in magic-angle twisted bilayer graphene, Nature (London) **582**, 198 (2020).
[22] U. Zondiner, A. Rozen, D. Rodan-Legrain, Y. Cao, R. Queiroz, T. Taniguchi, K. Watanabe, Y. Oreg, F. von Oppen, A. Stern, E. Berg, P. Jarillo-Herrero, and S. Ilani, Cascade of Phase Transitions and Dirac Revivals in Magic Angle Graphene, Nature (London) **582**, 203 (2020).
[23] Y. Saito, J. Ge, K. Watanabe, T. Taniguchi, and A. F. Young, Independent superconductors and correlated insulators in twisted bilayer graphene, Nat. Phys. **16**, 926 (2020).
[24] Y. Cao, D. Rodan-Legrain, J. M. Park, F. N. Yuan, K. Watanabe, T. Taniguchi, R. M. Fernandes, L. Fu, and P. Jarillo-Herrero, Nematicity and competing orders in superconducting magic-angle graphene, arXiv:2004.04148.
[25] C. L. Tschirhart, M. Serlin, H. Polshyn, A. Shragai, Z. Xia, J. Zhu, Y. Zhang, K. Watanabe, T. Taniguchi, M. E. Huber, and A. F. Young, Imaging orbital ferromagnetism in a moire Chern insulator, arXiv:2006.08053.
[26] C. Xu and L. Balents, Topological Superconductivity in Twisted Multilayer Graphene, Phys. Rev. Lett. **121**, 087001 (2018).
[27] J. Kang and O. Vafek, Symmetry, Maximally Localized Wannier States, and a Low-Energy Model for Twisted Bilayer Graphene Narrow Bands, Phys. Rev. X **8**, 031088 (2018).
[28] M. Koshino, N. F. Q. Yuan, T. Koretsune, M. Ochi, K. Kuroki, and L. Fu, Maximally Localized Wannier Orbitals and the Extended Hubbard Model for Twisted Bilayer Graphene, Phys. Rev. X **8**, 031087 (2018).
[29] H. C. Po, L. Zou, A. Vishwanath, and T. Senthil, Origin of Mott Insulating Behavior and Superconductivity in Twisted Bilayer Graphene, Phys. Rev. X **8**, 031089 (2018).
[30] C.-C. Liu, L.-D. Zhang, W.-Q. Chen, and F. Yang, Chiral Spin Density Wave and $d + id$ Superconductivity in the Magic-Angle-Twisted Bilayer Graphene, Phys. Rev. Lett. **121**, 217001 (2018).
[31] F. Wu, A. H. MacDonald, and I. Martin, Theory of Phonon-Mediated Superconductivity in Twisted Bilayer Graphene, Phys. Rev. Lett. **121**, 257001 (2018).
[32] Hiroki Isobe, Noah F. Q. Yuan, and Liang Fu, Unconventional Superconductivity and Density Waves in Twisted Bilayer Graphene, Phys. Rev. X **8**, 041041 (2018).
[33] H. Guo, X. Zhu, S. Feng, and R. T. Scalettar, Pairing symmetry of interacting fermions on a twisted bilayer graphene superlattice, Phys. Rev. B **97**, 235453 (2018).
[34] F. Guinea and N. R Walet, Electrostatic effects, band distortions, and superconductivity in twisted graphene bilayers, Proc. Natl. Acad. Sci. U.S.A. **115**, 13174 (2018).
[35] A. Thomson, S. Chatterjee, S. Sachdev, and M. S. Scheurer, Triangular antiferromagnetism on the honeycomb lattice of twisted bilayer graphene, Phys. Rev. B **98**, 075109 (2018).
[36] J. F. Dodaro, S. A. Kivelson, Y. Schattner, X. Q. Sun, and C. Wang, Phases of a phenomenological model of twisted bilayer graphene, Phys. Rev. B **98**, 075154 (2018).
[37] L. Zou, H. C. Po, A. Vishwanath, and T. Senthil, Band structure of twisted bilayer graphene: Emergent symmetries, commensurate approximants, and Wannier obstructions, Phys. Rev. B **98**, 085435 (2018).
[38] M. Ochi, M. Koshino, and K. Kuroki, Possible correlated insulating states in magic-angle twisted bilayer graphene under strongly competing interactions, Phys. Rev. B **98**, 081102(R) (2018).
[39] L. Rademaker and P. Mellado, Charge-transfer insulation in twisted bilayer graphene, Phys. Rev. B **98**, 235158 (2018).
[40] L. Balents, General continuum model for twisted bilayer graphene and arbitrary smooth deformations, SciPost Phys. **7**, 48 (2019).
[41] J. Ahn, S. Park, and B.-J. Yang, Failure of Nielsen-Ninomiya Theorem and Fragile Topology in Two Dimensional Systems with Space-Time Inversion Symmetry: Application to Twisted Bilayer Graphene at Magic Angle, Phys. Rev. X **9**, 021013 (2019).
[42] Z. Song, Z. Wang, W. Shi, G. Li, C. Fang, and B. A. Bernevig, All Magic Angles in Twisted Bilayer Graphene are Topological, Phys. Rev. Lett. **123**, 036401 (2019).
[43] K. Hejazi, C. Liu, H. Shapourian, X. Chen, and L. Balents, Multiple topological transitions in twisted bilayer graphene near the first magic angle, Phys. Rev. B **99**, 035111 (2019).
[44] J. Liu, J. Liu, and X. Dai, The pseudo-Landau-level representation of twisted bilayer graphene: Band topology and the implications on the correlated insulating phase, Phys. Rev. B **99**, 155415 (2019).
[45] J. W. F. Venderbos and R. M. Fernandes, Correlations and electronic order in a two-orbital honeycomb lattice model for twisted bilayer graphene, Phys. Rev. B **98**, 245103 (2018).
[46] J. Gonzalez and T. Stauber, Kohn-Luttinger Superconductivity in Twisted Bilayer Graphene, Phys. Rev. Lett. **122**, 026801 (2019).
[47] G. Tarnopolsky, A. J. Kruchkov, and A. Vishwanath, Origin of Magic Angles in Twisted Bilayer Graphene, Phys. Rev. Lett. **122**, 106405 (2019).
[48] J. Kang and O. Vafek, Strong Coupling Phases of Partially Filled Twisted Bilayer Graphene Narrow Bands, Phys. Rev. Lett. **122**, 246401 (2019).
[49] K. Seo, V. N. Kotov, and B. Uchoa, Ferromagnetic Mott State in Twisted Graphene Bilayers at the Magic Angle, Phys. Rev. Lett. **122**, 246402 (2019).
[50] S. Carr, S. Fang, Z. Zhu, and E. Kaxiras, Exact continuum model for low-energy electronic states of twisted bilayer graphene, Phys. Rev. Research **1**, 013001 (2019).
[51] Y.-H. Zhang, D. Mao, Y. Cao, P. Jarillo-Herrero, and T. Senthil, Nearly flat Chern bands in moire superlattices, Phys. Rev. B **99**, 075127 (2019).
[52] Q.-K. Tang, L. Yang, D. Wang, F.-C. Zhang, and Q.-H. Wang, Spin-triplet f-wave pairing in twisted bilayer graphene near $\frac{1}{4}$-filling, Phys. Rev. B **99**, 094521 (2019).
[53] J. Y. Lee, E. Khalaf, S. Liu, X. Liu, Z. Hao, P. Kim, and A. Vishwanath, Theory of correlated insulating behavior and spin-triplet superconductivity in twisted double bilayer graphene, Nat. Commun. **10**, 1 (2019).

[54] B. Roy and V. Juričić, Unconventional superconductivity in nearly flat bands in twisted bilayer graphene, Phys. Rev. B **99**, 121407(R) (2019).

[55] P. Lucignano, D. Alfé, V. Cataudella, D. Ninno, and G. Cantele, Crucial role of atomic corrugation on the flat bands and energy gaps of twisted bilayer graphene at the magic angle $\theta \sim 1.08°$, Phys. Rev. B **99**, 195419 (2019).

[56] X.-C. Wu, A. Keselman, C.-M. Jian, K. A. Pawlak, and C. Xu, Ferromagnetism and spin-valley liquid states in moire correlated insulators, Phys. Rev. B **100**, 024421 (2019).

[57] Y.-P. Lin and R. M. Nandkishore, Chiral twist on the high-T_c phase diagram in Moiré heterostructures, Phys. Rev. B **100**, 085136 (2019).

[58] Y. H. Zhang, H. C. Po, and T. Senthil, Landau level degeneracy in twisted bilayer graphene: Role of symmetry breaking Phys. Rev. B **100**, 125104 (2019).

[59] S. Liu, E. Khalaf, J. Y. Lee, and A. Vishwanath, Nematic topological semimetal and insulator in magic angle bilayer graphene at charge neutrality, arXiv:1905.07409 [Phys. Rev. Research (to be published)].

[60] Y. Alavirad and J. D. Sau, Ferromagnetism and Its Stability from the One-Magnon Spectrum in Twisted Bilayer Graphene, arXiv:1907.13633 [Phys. Rev. Lett. (to be published)].

[61] J. Liu and X. Dai, Correlated insulating states and the quantum anomalous Hall phenomena at all integer fillings in twisted bilayer graphene, arXiv:1911.03760.

[62] F. Wu and S. Das Sarma, Collective Excitations of Quantum Anomalous Hall Ferromagnets in Twisted Bilayer Graphene, Phys. Rev. Lett. **124**, 046403 (2020).

[63] M. Xie and A. H. MacDonald, Nature of the Correlated Insulator States in Twisted Bilayer Graphene, Phys. Rev. Lett. **124**, 097601 (2020).

[64] N. Bultinck, S. Chatterjee, and M. P. Zaletel, Mechanism for Anomalous Hall Ferromagnetism in Twisted Bilayer Graphene, Phys. Rev. Lett. **124**, 166601 (2020).

[65] C. Repellin, Z. Dong, Y.-H. Zhang, and T. Senthil, Ferromagnetism in Narrow Bands of Moire Superlattices, Phys. Rev. Lett. **124**, 187601 (2020).

[66] S. Chatterjee, N. Bultinck, and M. P. Zaletel, Symmetry breaking and skyrmionic transport in twisted bilayer graphene, Phys. Rev. B **101**, 165141 (2020).

[67] N. Bultinck, E. Khalaf, S. Liu, S. Chatterjee, A. Vishwanath, and M. P. Zaletel, Ground State and Hidden Symmetry of Magic Angle Graphene at Even Integer Filling, Phys. Rev. X **10**, 031034 (2020).

[68] D. V. Chichinadze, L. Classen, and A. V. Chubukov, Nematic superconductivity in twisted bilayer graphene, Phys. Rev. B **101**, 224513 (2020).

[69] Y. Zhang, K. Jiang, Z. Wang, and F. C. Zhang, Correlated insulating phases of twisted bilayer graphene at commensurate filling fractions: A Hartree-Fock study, Phys. Rev. B **102**, 035136 (2020).

[70] J. Kang and O. Vafek, Non-Abelian Dirac node braiding and near-degeneracy of correlated phases at odd integer filling in magic angle twisted bilayer graphene, Phys. Rev. B **102**, 035161 (2020).

[71] T. Cea and F. Guinea, Band structure and insulating states driven by Coulomb interaction in twisted bilayer graphene, Phys. Rev. B **102**, 045107 (2020).

[72] Y. D. Liao, J. Kang, C. N. Breio, X. Y. Xu, H.-Q. Wu, B. M. Andersen, R. M. Fernandes, and Z. Y. Meng, Correlation-induced insulating topological phases at charge neutrality in twisted bilayer graphene, arXiv:2004.12536.

[73] D. V. Chichinadze, L. Classen, and A. V. Chubukov, Orbital antiferromagnetism, nematicity, and density wave orders in twisted bilayer graphene, Phys. Rev. B **102**, 125120 (2020).

[74] R. M. Fernandes and J. W. F. Venderbos, Nematicity with a twist: Rotational symmetry breaking in a Moiré superlattice, Sci. Adv. **6**, eaba8834 (2020).

[75] L. Balents, C. R. Dean, D. K. Efetov, and A. F. Young, Superconductivity and strong correlations in Moiré flat bands, Nat. Phys. **16**, 725 (2020).

[76] E. Brillaux, D. Carpentier, A. A. Fedorenko, and L. Savary, Nematic insulator at charge neutrality in twisted bilayer graphene, arXiv:2008.05401.

[77] T. Soejima, D. E. Parker, N. Bultinck, J. Hauschild, and M. P. Zaletel, Efficient simulation of Moire materials using the density matrix renormalization group, Phys. Rev. B **102**, 205111 (2020).

[78] B. M. Hunt *et al.*, Direct measurement of discrete valley and orbital quantum numbers in bilayer graphene, Nat. Commun. **8**, 948 (2017); see Table I in the SI.

[79] Y. Ren *et al.*, WKB estimate of bilayer graphene's magic twist angles, arXiv:2006.13292.

[80] S. Becker *et al.*, Mathematics of magic angles in a model of twisted bilayer graphene, arXiv:2008.08489.

[81] N. N. T. Nam and M. Koshino, Lattice relaxation and energy band modulation in twisted bilayer graphene, Phys. Rev. B **96**, 075311 (2017).

[82] See Supplemental Material at http://link.aps.org/supplemental/10.1103/PhysRevLett.125.257602 for details of the derivation of the RG equations, RG evolution of the sublattice polarization and Wilson loop eigenvalues, as well as the single particle excitation spectrum in the strong coupling.

[83] I. F. Herbut, Quantum Critical Points with the Coulomb Interaction and the Dynamical Exponent: When and Why $z = 1$ Phys. Rev. Lett. **87**, 137004 (2001); although there are nonlogarithmic corrections to the dielectric *function*, whose full consideration is beyond the scope of this work, they do not change the main conclusions.

[84] H. Watanabe, Counting rules of Nambu-Goldstone modes, Annu. Rev. Condens. Matter Phys. **11**, 169 (2020).